KSME

Springer

Journal of Mechanical Science and Technology 36 (11) 2022

Original Article
DOI 10.1007/s12206-022-1018-5

Keywords:
· Planar jet
· Moving surface
· Interface
· Turbulence
· Heat transfer

Correspondence to:
Jinkee Lee
lee.jinkee@skku.edu

Citation:
Baghel, K., Zahra, Lee, J. (2022). Free surface planar liquid jet impingement on a moving surface: interfacial flow and heat transfer characteristics. Journal of Mechanical Science and Technology 36 (11) (2022) 5537~5549.
http://doi.org/10.1007/s12206-022-1018-5

Received April 12th, 2022
Revised July 13th, 2022
Accepted July 29th, 2022

† Recommended by Editor Han Seo Ko

Free surface planar liquid jet impingement on a moving surface: interfacial flow and heat transfer characteristics

Kuldeep Baghel[1], Zahra[1] and Jinkee Lee[1,2]

[1]School of Mechanical Engineering, Sungkyunkwan University, Suwon 16419, Korea, [2]Institute of Quantum Biophysics, Sungkyunkwan University, Suwon 16419, Korea

Abstract Understanding heat transfer characteristics of sheet metal is of practical importance in sheet metal rolling operation to ensure strength and quality of final product. We present a numerical study of free surface planar liquid jet impingement on a uniformly heated moving surface. Scale adaptive simulation (SAS) for turbulent flow and volume of fluid (VOF) method was used to capture the liquid-air interface. The computational domain was divided into two parts to carry out 3D simulations, then results of separate domains were superimposed to resolve boundary conditions. A parametric study considered three different jet Reynolds numbers of 4000, 8000 and 12000. Four different surface to jet velocity ratios, u_s/u_j, were considered. We focused on studying interfacial flow characteristics, turbulence intensity variations, and their relation to heat transfer. Splitting the domain into two parts and superimposing results as boundary conditions resulted in a reasonable accuracy and reduced computation cost. We observed that gravity significantly affects interfacial structures at Reynolds number of 4000. As surface velocity increases, the heat removal rate from the impingement surface in the direction of plate motion increases. However, contrasting trends are observed in the reverse direction despite increased turbulence fluctuations with surface velocity.

1. Introduction

Jet Impingement cooling is used where localized high heat removal rate is desired. This technique has applications in electronics cooling, turbine blade cooling, tampering of glasses etc. Studies of heat transfer from moving components and flow structures are of practical importance in manufacturing and material processing such as metal extrusion, casting, paper drying, metal forming, rolling of hot metals [1-3]. In sheet metal rolling operation, hot metal sheets are cooled by water liquid [4, 5], where the liquid is generally supplied over the hot surface in the form of a planar jet, circular jet, or spray. The cooling rate of hot metal sheets during sheet metal rolling governs the strength and quality of sheet metal [6-8]. Xu et al. [6] have investigated the effect of cooling rate on the hardness, tensile strength, and grain structures for aluminum alloy sheets. Similarly, Lobanov et al. [8] have investigated the effect of cooling rate on low carbon steel alloy.

In studies of moving surfaces subjected to air or liquid jet, the focus has been given to quantifying the heat transfer coefficient of the impingement surface and its dependency on moving surface motion and Reynolds number of the jet. In numerical studies of jet impingement on a moving surface, the air or a submerged liquid jet was investigated. To model the effect of turbulence fluctuations, $k-\epsilon$ [9, 10], $k-\omega$ [11], v^2-f [12], shear stress transport (SST) $k-\omega$ [13] and transition *SST* [14] models were used for numerical studies of impinging jet considering moving surface. Mohaghegh and Rahimi [15] have used a similarity solution approach to resolve heat transfer characteristics of water jet impingement on the moving surface using laminar flow assumption. Chattopadhyay et al. [16] performed LES simulation for slot jet impingement on a moving surface. Shah [13] and Chitsazan and Glasmacher [17] have considered multiple jets in

their study. Pawar and Patel [11] investigated the effect of jet inclination and the moving surface motion on heat transfer characteristics for air-jet impingement.

Shah [13] has shown that increasing surface velocity reduces stagnation Nusselt number. Similar observations were made in other studies of moving surfaces subjected to impinging jets [16, 18]. Varying the surface velocity to a more extensive range, it was shown that local and average heat transfer coefficient first decreases with increasing surface velocity until a specific critical value; it starts to increase with further increase of surface velocity [9, 12]. Chattopadhyay et al. [16] have shown that a more uniform temperature distribution can be achieved with higher surface velocity. Likewise, Kadiyala and Chattopadhyay [14] have shown that the heat transfer of a fast-moving surface was significantly higher than the static surface case. For moving surfaces, the effect of transient velocity was also analyzed by Ersayin and Selimefendigil [19]. Similarly, the effect of moving nozzle was investigated by Rahimi and Azimi [20] in unconfined jet configuration. They have shown that moving nozzles with fast speed has a deteriorating effect on heat transfer.

To reduce heat load from the heated moving surface, the effects of nanofluids were investigated. Manca et al. [10] performed 2D numerical simulations using, $k-\epsilon$ turbulence model for understanding the effect of nanofluids and moving surface subjected to slot jet impingement in confined configuration. They concluded that surface velocity and nanofluid's combined effect increase moving surfaces' local and average heat transfer coefficient. Similarly, using a laminar assumption Basaran and Selimefendigil [18] have performed a numerical study considering the properties of Al_2O_3 nanofluid and water liquid in their study of slot jets on a moving surface. Likewise, Cosanay et al. [21] have used multiple slot jets and moving hot surface subjected to nanofluid jet impact in confined configurations.

Two kinds of boundary conditions were used for outer boundaries in the literature on impinging jets considering moving surfaces. First is the zero gradient boundary condition where gradients of flow variables are assumed to be zero normal to boundary [11, 19, 22]. The zero gradient boundary condition could produce unrealistic results since the moving surface would induce shear-driven flow near the boundary and cause formations of vortices near the boundary. The majority of studies adopted pressure outlet boundary conditions for static surface cases, where pressure was assumed to be constant at ambient conditions [10, 12, 13, 23-25]. In constant pressure boundary, the domain should be sufficiently large in the opposite direction of surface velocity so that the effect of boundary on flow would be insignificant for moving surface case. Creating a larger domain could be computationally time-consuming and expensive. In numerical studies of moving surfaces subjected to impinging jet, a modified pressure outlet boundary condition is adopted in a few studies, where the pressure was specified as weighted average considering nearest neighbor cell of boundary and ambient pressure [16, 20, 26-28]. Weighted average boundary condition may produce reasonably better results than constant pressure or ambient pressure boundary condition. However, impingement jet is a turbulent phenomenon and reverse flow at boundary could significantly affect heat transfer characteristics. To address this issue, some alternative approach is required for numerical studies.

Studies have been primarily conducted for air-jet or liquid jets in confined configurations in literature. However, given the hot metal rolling operation, analysis involving free interface would be of more practical significance. To the authors' best knowledge, no numerical study is available for the free surface planar liquid jet impingement on a moving surface that discusses interfacial flow and heat transfer characteristics. Resolving the outer boundary is crucial for such cases due to the involvement of liquid film. In the free surface liquid jet, phenomena is complicated due to interfacial structures, and turbulence fluctuations [29, 30]. We hypothesize that moving surfaces would significantly affect turbulence fluctuations and convective heat transfer from the heated moving surface. The other aspect is that moving surface also hinder direct interaction of the liquid with the impingement surface and subsequently affect the heat transfer characteristics and interfacial structures. Also, due to reverse flow at boundaries owing to surface motion, the extent of the computation domain might affect the accuracy of numerical simulation. This suggests that special treatment is required for boundary condition to improve accuracy of numerical studies.

This work presents a numerical study of free surface liquid jet impingement on a uniformly heated moving surface. We used domain splitting and superimposing phenomena to overcome the limitations and drawbacks of previously used outer boundary conditions in literature. In this approach, we have divided a large computation domain into two smaller domains and performed computational simulation separately. We need to design these two domains so that some portion of the smaller domain's overlaps. Results of separate domain simulations corresponding to overlapping regions are used as the boundary conditions for numerical simulations. In other words, we are dividing larger geometry into overlapping smaller geometries to carry out the numerical simulation. This kind of approach can be utilized for a broad range of problems in fluid mechanics and other computational fields after validation.

2. Numerical procedure

In the case of air-jet impingement, SST $k-\omega$ model has shown better prediction capability of heat transfer characteristics than other turbulence models [13, 31]. In our previous work [32], we showed that this model predicts heat transfer characteristics better as compared to other RANS models [32, 33]. Similar observations were made by Maliska et al. [34]. SST-SAS model was developed by Egorov and Menter [35]. Further details of model coefficients and other information can be found in papers by Menter et al. [36] and Menter and Egorov [37]. SST-*SAS* model is the improvement of the SST $k-\omega$ model. In governing equations of SST $k-\omega$ model, an addi-

tional production source term is introduced to ω equation to resolve unsteady fluctuations. The Von Korman length scale was introduced to resolve temporal and spatial scales in this model. SST-*SAS* model behaves similar to *LES* in regions of unsteadiness, whereas in the smooth region, it results in RANS-like predictions [38].

2.1 Governing equations

To simulate interfacial flow phenomena, VOF method is used. Eq. (1) shows volume fraction equation [39].

$$\frac{1}{\rho_w}\left[\frac{\partial}{\partial t}\left(\alpha_w\rho_w\right)+\nabla.\left(\alpha_w\rho_w\bar{u}_{wi}\right)=+\sum_{p=1}^{n}\left(\dot{m}_{aw}-\dot{m}_{wa}\right)\right] \tag{1}$$

In above equation, superscript *w* represents water and *a* present air phase. Volume fraction for air phase is deterimned by Eq. (2).

$$\alpha_w+\alpha_a=1 \tag{2}$$

Mixture properties, Pro_{mix}, in computational domain is determined by Eq. (3).

$$Pro_{mix}=\alpha_w Pro_w+\left(1-\alpha_a\right)Pro_a \tag{3}$$

Time averaged RANS equations is presented by Eq. (4) in tensor notation form.

$$\rho\bar{u}_j\frac{\partial\bar{u}_i}{\partial x_j}=\frac{\partial}{\partial x_j}\left[-\bar{p}\delta_{ij}+\mu\left(\frac{\partial\bar{u}_i}{\partial x_j}+\frac{\partial\bar{u}_j}{\partial x_i}\right)-\rho\overline{u_i'u_j'}\right] \tag{4}$$

To model the effect of surface tension, source terms presented by Eq. (5) [40] is added in Eq. (4).

$$F_{\text{vol}}=\sigma_{aw}\frac{\rho\kappa\nabla\alpha_a}{\frac{1}{2}\left(\rho_a+\rho_w\right)},\ \kappa=\nabla.\hat{n},\ \hat{n}=\frac{n}{|n|} \tag{5}$$

σ_{aw} is surface tension for air water interface. Time averaging of Navier Stokes equations results in unknown terms ($\rho\overline{u_i'u_j'}$) as shown in Eq. (4). To model these terms, SST-SAS model is used in present study. Mathematically it differs by SST *k*−*ω* model by a source term in *ω* equation of SST *k*−*ω* model. *ω* equation of SST-SAS model is given by Eq. (6).

$$\begin{aligned}\frac{\partial\omega}{\partial t}+U_j\frac{\partial\omega}{\partial x_j}&=\alpha S^2-\beta\omega^2+\frac{\partial}{\partial x_j}\left[\left(\nu+\sigma_\omega\nu_T\right)\frac{\partial\omega}{\partial x_j}\right]\\&+2\left(1-F_1\right)\sigma_{\omega2}\frac{1}{\omega}\frac{\partial k}{\partial x_i}\frac{\partial\omega}{\partial x_i}+Q_{SAS}\end{aligned} \tag{6}$$

The source term in SST-*SAS* model is based on Rotta transport equations [35-37]. Eq. (7) gives the source term.

$$\begin{aligned}Q_{\text{SAS}}&=\rho\times max[\zeta_2\kappa S^2\left(\frac{L}{L_{\text{vK}}}\right)^2\\&-C\frac{2k}{\sigma_\Phi}max\left(\frac{1}{\omega^2}\frac{\partial\omega}{\partial x_i}\frac{\partial\omega}{\partial x_i},\frac{1}{k^2}\frac{\partial k}{\partial x_i}\frac{\partial k}{\partial x_i}\right),0]\end{aligned} \tag{7}$$

Model constants are given as:

$$\zeta_2=3.51,\ \sigma_\Phi=2/3,\ C=2 \tag{8}$$

Length scale, *L* is given by Eq. (9)

$$L=\sqrt{k}/\left(c_\mu^{1/4}\times\omega\right),\ c_\mu=0.09 \tag{9}$$

L_{vK} is Von Karmon length scale can be presented as:

$$L_{\text{vK}}=\frac{\kappa S}{\left|\nabla^2U\right|},\ \left|\nabla^2U\right|=\sqrt{\left(\nabla^2u\right)^2+\left(\nabla^2v\right)^2+\left(\nabla^2w\right)^2} \tag{10}$$

To control the damping of small scale resolved turbulence fluctuations, a lower limit is applied to L_{vK} and is given as:

$$L_{\text{vK}}=max\left(L_{\text{vK}},C_s\times\sqrt{\frac{\zeta_2\kappa}{\left(\beta/c_\mu\right)-\alpha}}\times\Delta\right),\ C_S=0.11 \tag{11}$$

In above equation, the second term in the bracket is proportional to element size, Δ ($\Delta=\Omega_{cv}^{(1/3)}$), in computational domain. Here, Ω_{cv} represent the control volume. Further, details of the SST-SAS model can be found in Refs. [35, 37]. Eq. (12) shows the time-averaged energy equation.

$$\frac{\partial\bar{T}}{\partial t}+\bar{u}_i\frac{\partial\bar{T}}{\partial x_i}=\alpha\frac{\partial^2\bar{T}}{\partial x_i\partial x_i}-\frac{\partial\overline{u_i'T'}}{\partial x_i} \tag{12}$$

Similar to Reynolds stresses, unknown terms in Eq. (12) can be presented as a function of temperature gradient and turbulent Prandtl number.

$$-\overline{u_i'T'}=\alpha_t\frac{\partial\bar{T}}{\partial x_i},\ \alpha_t=\frac{\nu_t}{Pr_t}.$$

2.2 Computational domain

Fig. 1(a) shows computational domain, boundary conditions and dimensions. Color codes describe different faces and boundaries of geometry considered for simulation. The bottom boundary, indicated as a moving surface in Fig. 1(a), represents a uniformly constant heat flux (q'' = 150 kW/m^2) surface moving with a constant velocity in the positive z-direction. Origin (x = y = z = 0), is the geometric center. The zy plane is assigned as the symmetry plane.

Except for the right boundary (z = -40 mm), all other outer boundaries are assumed to be at ambient conditions, and pressure outlet condition is applied at those faces. Velocity at nozzle exit or inlet of the present domain was based on nozzle Reynolds number. Table 1 summarizes the boundary parameters such as mean jet velocity and surface velocity considered for present study. The boundary at z = -40 mm, described as pressure outlet or inlet in Fig. 1(a), needs special treatment since the impingement surface moves in the positive z-direction. The moving surface will drag the outer liquid to the computational domain, which could significantly affect the simulation outcome. The velocity, temperature, and other turbulence variables are unknown before the simulation at this boundary. To resolve this issue, either the computational domain should be sufficiently long in negative z-direction, or reasonable velocity and turbulence profiles should be applied at this face. Given the interfacial liquid film phenomena, a larger domain is out of the scope of the present study since the number of elements would increase significantly. A splitting domain approach is adopted to resolve this issue. As shown in Fig. 1(b), the computational domain is divided into two parts and represented by domain 1 and domain 2. The dimensions of Domain 1 are the same as presented in Fig. 1(a). In domain 1, P2' is assigned as pressure outlet boundary. Except for this face (P2'), all other boundary conditions are the same as described in Fig. 1(a). At the top of domain 1, the inlet boundary is the velocity inlet boundary, where fully developed velocity and turbulence variables are superimposed. A separate simulation for a sufficiently long slot nozzle, length 400 mm (*40 w*), is performed to get fully developed velocity and turbulence profiles [41, 42]. The resulting conditions are superimposed at the inlet boundary of domain 1. For clarity, see schematic at the top of domain 1 in Fig. 1(b). With these conditions, numerical simulations are carried out for domain 1. After convergence, velocity, turbulence intensity, and volume fraction profiles are extracted from plane P1, as symbolically shown in Fig. 1(b). We also extracted profiles from the plane at z = -20 mm. However, choosing the plane at z = -10 mm for superimposing profiles given better accuracy. Domain 2 (Fig. 1(b)) is a separate domain designed in a way that plane P1' and P2 coincides with plane P1 and P2', respectively. Overlapped or combined geometry can be considered a single computational domain with a sufficiently long geometric length in the negative z direction till z/d = -120 mm. Boundary conditions for domain 2 are the same as described boundary conditions in Fig. 1(a) except for the condition at face P1'. Also, nozzle inlet is not present in domain 2. Velocity, turbulence, and volume fractions variables are extracted from the simulation of domain 1, and are used as inlet boundary at face P1' in computational domain 2. Using these steps, numerical simulations are carried out for domain 2. The resulting flow variables at plane P2 are further extracted and superimposed on domain 1 at plane P2'.

Table 1. Boundary parameters in numerical study.

Re	u_j	u_s (u_s/u_j = 0)	u_s (u_s/u_j = 0.1)	u_s (u_s/u_j = 0.2)	u_s (u_s/u_j = 0.4)
4000	0.348	0	0.034	0.069	0.139
8000	0.696	0	0.069	0.139	0.278
12000	1.045	0	0.104	0.209	0.418

2.3 Solution method

Ansys Fluent is used for the computational study. A transient, pressure-based solver was chosen, and gravity was consid-

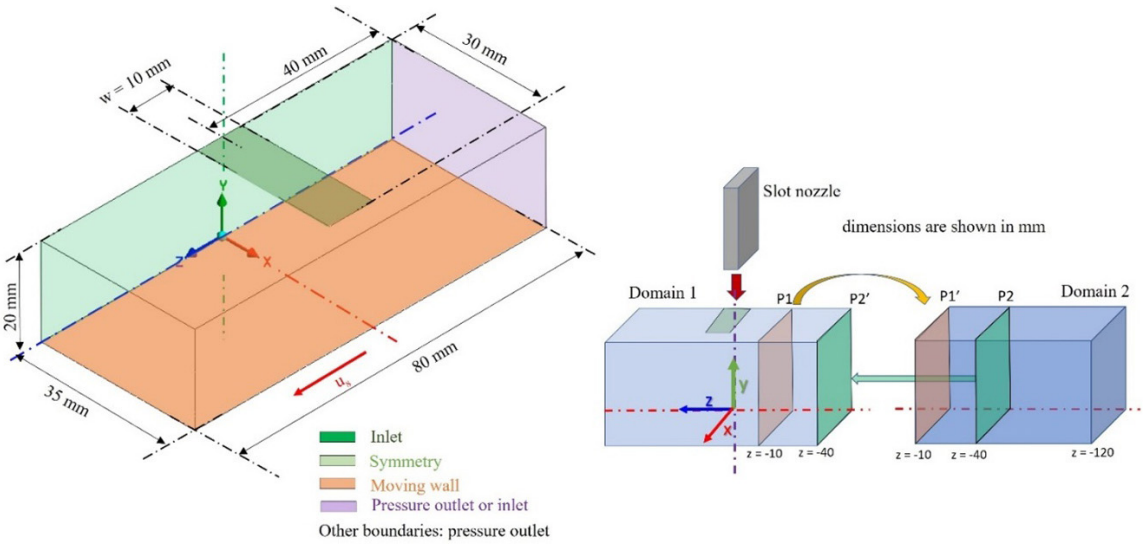

(a) (b)

Fig. 1. (a) Computational domain, boundary conditions, and dimensions of geometry; (b) domain splitting and resolving boundary conditions.

ered downward. Interface modeling was achieved using the implicit VOF method. Likewise, the implicit scheme was chosen for body force formulation. Two fluids, air and water, are considered for VOF simulation. Continuum surface force formulation with wall adhesion was adopted for surface tension force modeling. Properties of air and water are considered at nozzle exit temperature of T = 298.16 K and shown in Table 2. We observed that the results are independent of contact angle choice since the contact line will be beyond the extent of domain size considered here. The surface tension value of 0.0731 N/m was used for numerical simulation. Transient numerical simulation was performed using the time step size of 0.0001 s. For every time step, twenty iterations were performed. Residuals criteria were set to 10^{-5} for continuity and 10^{-6} for momentum, turbulence, and volume fraction equations. These criteria were successfully satisfied during the numerical calculations. The transient profile of average Nusselt number is observed during simulations. When the variations in average Nusselt number become negligible, solutions were considered at the steady state. Computations were carried out using 2.30 GHz Intel (R) Xeon (R) CPU E5-2697v4 processor with 128 GB RAM. For one case, numerical simulation has taken around 160 hours, including both domain and slot nozzle simulations. For the case of Re = 12000 (u_s/u_j = 0.4), after 0.3 second solution has achieved steady state. Steady state time was found to be different for different cases.

2.4 Validation and grid sensitivity

Fig. 1 shows the meshing of the computational domain. We have used cut cell meshing to generate the cells of the aspect ratio closer to 1 in most of the computational domains. Refined elements were created at the inlet boundary, expected liquid and interface flow zone. Element sizes at the inlet boundary are 225 μm, and it is 450 μm in the highlighted region above inflation layers. Element sizes increase towards the expected air zone in computational domain as clear from Fig. 2. The first cell height was 10 microns with a 1.5 factor of growth rate. To satisfy the model y^+ condition, a total of 10 layers were created near the wall.

To check the validity of proposed method and error quantification, extreme case of present study (Re = 12000, u_s/u_j = 0.4) is simulated using extended domain considering 120 mm of domain extent in reverse direction using pressure outlet boundary condition. Here, extended domain simulation is carried out using the element size of 700 μm instead of 450 μm due to limitations in computational resources and high computational cost. The results using alternate boundary conditions as described earlier and extended domain cases are compared to check the suitability of numerical simulations as shown in Fig. 3(a). This figure also presents the results of the grid independence study. Qualitatively, the result matches well for limited

Table 2. Fluid properties considered for numerical simulation.

Fluid	ρ(kg/m^3)	μ(kg/m·s)	c_p(J/kg·K)	k(W/m·K)	Pr
Water	996.58	0.0008680	4072.7	0.61229	5.7763
Air	1.1845	1.84 × 10^{-5}	1006.3	0.025969	0.71465

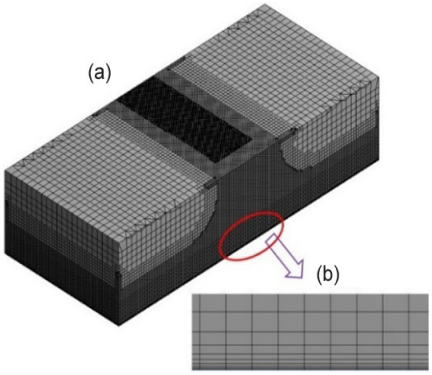

Fig. 2. Grid size distributions in computational domain.

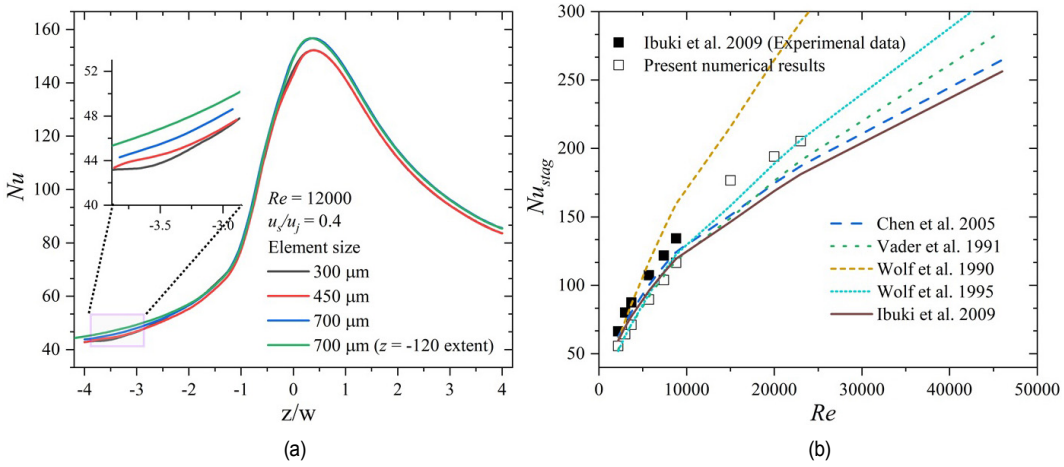

Fig. 3. (a) Grid independence study and validity of domain splitting and superimposing boundary condition approach; (b) comparison of Nusselt number at the stagnation point in the literature.

Table 3. Correlations to predict stagnation Nusselt number for free surface liquid jet impingement.

Correlation	Reference
$Nu_{stag} = 0.634 Re_j^{0.5} Pr^{0.38}$	Chen et al. [45]
$Nu_{stag} = 0.634 Re_j^{0.58} Pr^{0.4}$	Vader et al. [44]
$Nu_{stag} = 0.634 Re_j^{0.71} Pr^{0.4}$	Wolf et al. [46]
$Nu_{stag} = 0.634 Re_j^{0.62} Pr^{0.4}$	Wolf et al. [30]
$Nu_{stag} = 0.634 Re_j^{0.5} Pr^{0.33}$	Ibuki et al. [43]

and extended domain cases. The minor difference in local Nusselt number values could be attributed to different element sizes in both cases, along with the error introduced by superimposing phenomena. These results confirm the suitability of the proposed boundary conditions. At the same time, these results also confirm domain and grid independence. Comparing results of different element sizes suggest that the grid size of 450 μm gird is suitable for further study.

Fig. 3(b) compares Nusselt numbers at the stagnation point with the data predicted by correlations and experimental data available in the literature for static surface cases. Table 3 shows the details of correlations. These correlations are based on Reynolds and Prandtl numbers at nozzle exit conditions. It should be noted that the numerical data for cases of Reynolds number below 10000 is presented for *Pr* number of 7 to match with the experimental conditions of Ibuki et al. [43]. Similarly, data for Reynolds number more than 10000 is presented for *Pr* number of 5.8 to match with the experimental conditions of Vader et al. [44]. The results compare reasonably well with the correlations and experimental data from the literature. Maximum error for the data below *Re* = 10000 is 15 % as compared to experimental data of Ibuki et al. [43]. However, for *Re* ≤ 10000, the error is below this figure as compared to prediction using correlations given in Refs. [30, 43, 45]. Given this comparison, the present numerical work can be extended to study free-surface liquid jet impingement on a moving surface.

3. Results and discussion

This section discusses interfacial flow features, turbulence fluctuations, and heat transfer effects. Further, a parametric study is presented to understand the effect of surface velocity and Reynolds number on interfacial characteristics and Nusselt number. Since the surface moves in the positive *z* direction, the forward region is the location on the impingement surface on the positive *z* axis, whereas the reverse region is the negative *z* axis region. Data are presented along the z-axis, $x = y = 0$, and symmetry plane ($x = 0$). The impact region is defined as the location near the geometric center where $-0.5 \le z/w \le 0.5$. *H* represents nozzle exit to impingement surface spacing.

3.1 Interfacial flow characteristics

In the VOF method, a particular fluid's presence at any location is determined by the volume fraction, *α,* value, which varies from zero to one. Zero indicates that the cell is occupied by air, and one represents that the cell is occupied by water only. Any value between zero and one represents the mixture phase. Fig. 4(a) shows the volume fraction contour at *yz* plane of the computational domain for static surface case of *Re* = 12000. As clear from Fig. 4(a), volume fraction values vary from zero to one within a small distance of the order of microns. The location corresponding to the 0.5 value of volume fraction is assumed interface location. Information of interface location is used to determine jet and film thickness for liquid jet impingement.

Jet thickness, j_t, can be defined as the distance between interface locations along *z* direction at the given value of *y* location, as shown in Fig. 4(a). Figs. 4(b)-(d) show the interface locations for Reynolds numbers of 4000, 8000 and 12000, respectively. For Reynolds number of *Re* = 4000, jet thickness reduces as jet moves towards the impingement surface till $y/w \approx 0.8$. Following this, the jet thickness increases downward due to the flow resistance by the impingement surface. For Reynolds number of *Re* = 12000 as depicted in Fig. 4(d), the jet thickness remains nearly constant till $y/w = 1.2$. It increases downward following this location. The interface locations have slight variations for the intermediate Reynolds number of *Re* = 8000 as shown in Fig. 4(c). From these observations, it can be concluded that the effect of gravity is dominant for the lower *Re* case.

The effect of surface velocities are also depicted in Figs. 4(b)-(d). The moving surface has a negligible effect on liquid jet thickness prior to impact irrespective of Reynolds numbers and surface velocities. This implies that the moving surface is influencing a narrow region near the impingement surface. The distance from the impingement surface to the interface located in the positive y-direction can be considered as liquid film thickness, f_t, as highlighted in Fig. 4(a). In case of *Re* = 4000 and static surface case, film thickness is nearly constant form location $z/w \approx 1$ to 2.7. Following this location, liquid film thickness increases until $z/w \approx 3.8$, and then it reduces slightly. A sudden increase in liquid film thickness for liquid jet impingement is termed as the hydraulic jump in the Refs. [47, 48]. The hydraulic jump occurs when a higher velocity liquid pushes a slower moving liquid in the flow direction. For all surface velocity cases, hydraulic jump phenomenon is observed for *Re* = 4000 in the forward region, $3 \le z/w \le 4$, and in the reverse region at $-4 \le z/w \le -3$. As clear from enlarged curves shown in Fig. 4(b), liquid film thickness increases by reducing surface velocities in the forward region. On the reverse side, liquid film thickness shows opposite trend till $z/w \approx -2.6$. Also, surface velocity significantly affects the hydraulic jump on the reverse region at $-4 \le z/w \le -2.6$. For $u_s/u_j = 0.1$ as depicted in Fig. 4(b), significantly lower liquid film thickness is observed in hydraulic jump location as compared to other cases. Physically moving

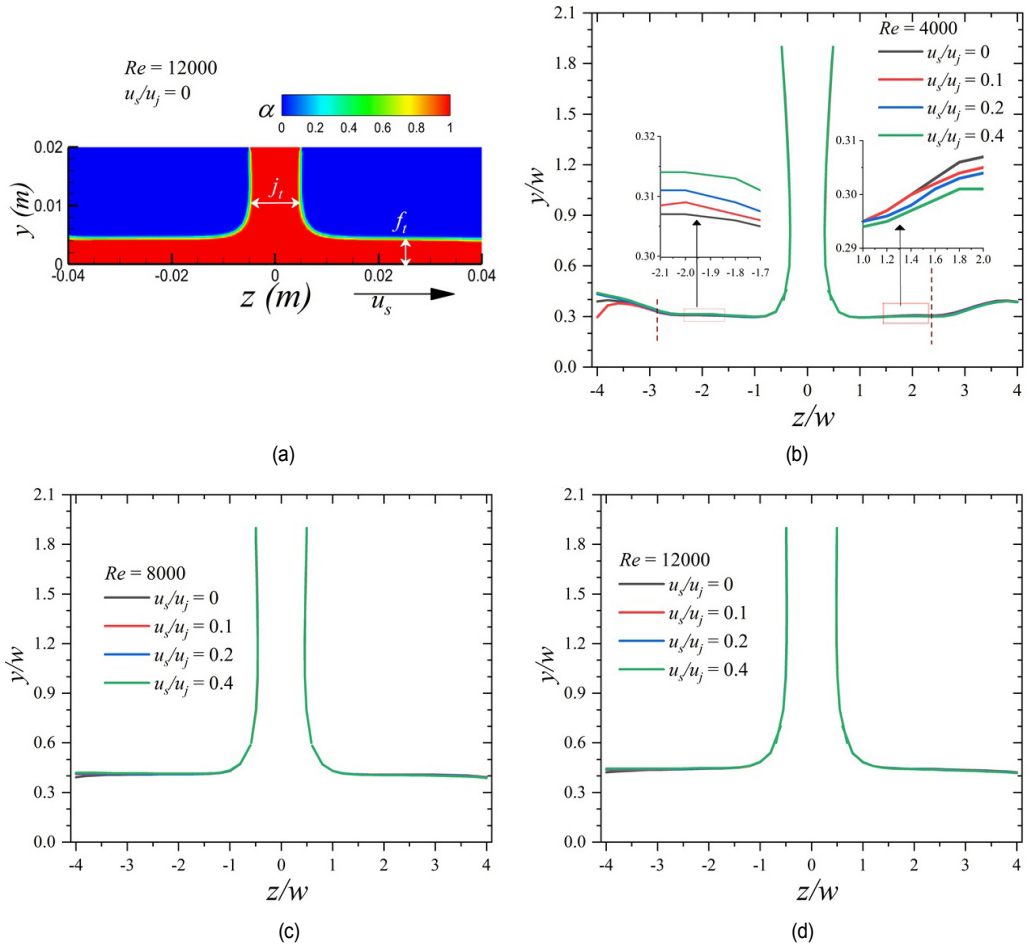

Fig. 4. (a) Volume fraction contours at the symmetry plane when *Re* = 12000, u_s/u_j = 0. The interfacial structures and their dependency on surface velocity and Reynolds number of (b) Re = 4000; (c) Re = 8000; (d) Re = 12000, inset of figure is enlarge interface profile for u_s/u_j.

surface pushing hydraulic jump towards the impact region. For the case of higher surface velocities of u_s/u_j = 0.2 and 0.4, more liquid is moving in the forward direction, causing liquid film thickness to be higher as compared to lower surface velocity cases. At other locations except hydraulic jump region, the difference in liquid film thickness for different surface velocity cases is marginal relative to static surface case.

As depicted in Figs. 4(c)-(d), the hydraulic jump is not observed for *Re* = 8000 and 12000. The hydraulic jump location moves away from the jet impact region with increasing Reynolds number [48]. On the reverse region, the surface velocity direction is opposite to fluid film movement, which results in reduced mean velocity of the liquid film. As a result, liquid film thickness increases owing to the conservation of the mass principle. In contrast, liquid film movement in the forward direction is supported by surface motion; hence, the overall mean velocity is higher, which subsequently reduces the liquid film thickness. Enlarge part of Fig. 4(b) showing this characteristic. Overall, the film thickness is higher in the reverse region as compared to thickness in the forward region, as is clarified by enlarged parts of curves in Fig. 4(b).

The effect of Reynolds number can also be observed on the jet or liquid film thickness from Figs. 4(b)-(d). The jet thickness increases with increasing Reynolds number due to the reduced effect of gravity for higher *Re* cases. The location after which jet thickness increases in a downward direction shift away from the impact region with the increase in Reynolds numbers. This was because more liquid mass will come out of the nozzle exit with the increase in Reynolds number. At the same time, the impingement surface provides resistance to flow, resulting in reduced velocity of the liquid jet before it comes to stagnation conditions. The presence of impingement surface will be felt earlier for higher velocity jet and higher *Re* case. Therefore, the thickness in the downward increase and it is higher for higher Reynolds number. At location $y/w \approx 0.8$, jet thickness for *Re* = 4000 is nearly 38 % lower than *Re* = 12000, indicating reduced effect of gravity for higher *Re* case. The trends of liquid film thickness for lower Reynolds numbers are significantly different from higher *Re* cases owing to hydraulic jump, as explained earlier. The difference between liquid film thickness between *Re* = 4000 and *Re* = 12000 is significant near the impact. However, the difference reduces as the liquid film moves away from the impact. Hydraulic jump phenomena, as discussed earlier, is responsible for increasing liquid film thickness away from the

impact for lower *Re*.

3.2 Turbulence intensity variations

For turbulent jets, fluctuations in velocity components could significantly affect heat transfer characteristics. Moreover, moving surfaces may enhance turbulence fluctuations. We analyzed turbulence intensity variations to understand these characteristics. Turbulence intensity, *I*, is defined as the ratio of root mean squire of turbulent velocity fluctuations $[u' \equiv \sqrt{\left(u_x'^2 + u_y'^2 + u_z'^2\right)/3}\,]$ and time-averaged mean velocity ($U \equiv \sqrt{U_x^2 + U_y^2 + U_z^2}$). Here, U_x, U_y and U_z are components of time-averaged mean velocity and u_x', u_y', u_z' are fluctuating components of velocities.

Figs. 5(a) and (b) show the turbulence intensity contours for static and moving surface cases for *Re* = 4000. Results are presented within the liquid region near the impingement surface at the symmetry plane. The turbulence intensity distribution is symmetric as expected at both sides of the geometric center for the static surface case. As the liquid flows downstream, away from the impact, a higher turbulence intensity level is observed, as shown and highlighted by the rectangular region along both sides. Similar observations were made for free surface circular jet impingement on a flat surface by Stevens and Webb [33, 49]. As clear from Fig. 5(b), for moving surface case of *Re* = 4000 and u_s/u_j = 0.4, significantly different turbulence characteristics can be observed. Higher turbulence intensity is observed on the reverse region than the forward region. Turbulence intensity profiles near the surface at *y* = 0.35 mm are shown in Fig. 5(c) for statics and moving surface. As depicted in the figure, turbulence intensity is around 41 % percent lower for moving surface cases in the forward region at *z*/*w* = 3, compared to the static surface case. However, it is 49 % percent higher in the reverse region at *z*/*w* = -3. In the forward region, surface velocity and liquid film movement both support the forward movement of the liquid film.

However, in the reverse region, the direction of the moving surface and the liquid coming from the nozzle has momentum in opposite directions. Moving surfaces whose velocity is in positive z-direction will drag liquid in the direction of surface velocity. In contrast, the liquid coming from the nozzle and having momentum in the negative z-direction will drag the liquid in the opposite direction. These motions of liquid layers may form vortices, and, as a result, higher turbulence fluctuations are observed on the reverse region. On the forward region, the moving surface supports liquid motion in the forward direction. Turbulence intensity on the forward region is lower due to a low-velocity gradient and the absence of reverse motion. Similar trends of turbulence intensity distribution were observed for higher Reynolds number cases.

3.3 Heat transfer characteristics

The present work calculates the local Nusselt number, non-dimensional heat transfer coefficient, by the following expression.

$$Nu = \frac{q'' d_h}{k_w \left(T_s - T_\infty\right)} \tag{13}$$

In the above expression, q'', is heat flux at the uniformly heated static or moving surfaces. T_s is the local temperature at the heated surface, and T_∞ is the temperature of water liquid at the nozzle exit. k_w is the conductivity of water at nozzle exit temperature and pressure (1 atm). Fig. 6(a) shows Nusselt number profiles along the z-axis (*x* = *y* = 0) at the impingement surface for static and moving surface cases at a fixed value of Reynolds number of 4000. For the static surface case, the maximum value of the Nusselt number is observed at the stagnation point or the geometric center. Following it, the Nusselt number decreases gradually and then sharply till *z*/*w* ≈ 1.5. In turbulence intensity distribution, as was shown in Fig. 5(c), it was observed that turbulence intensity values increase in liquid

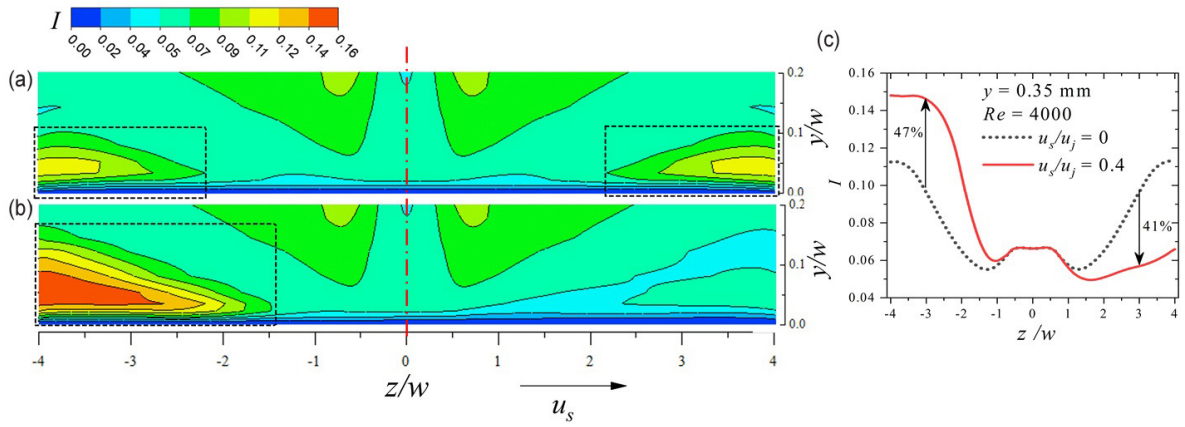

Fig. 5. Turbulence intensity contours for Re = 4000: (a) static surface; (b) moving surface; (c) turbulence intensity profiles near to the surface for static and moving surface cases.

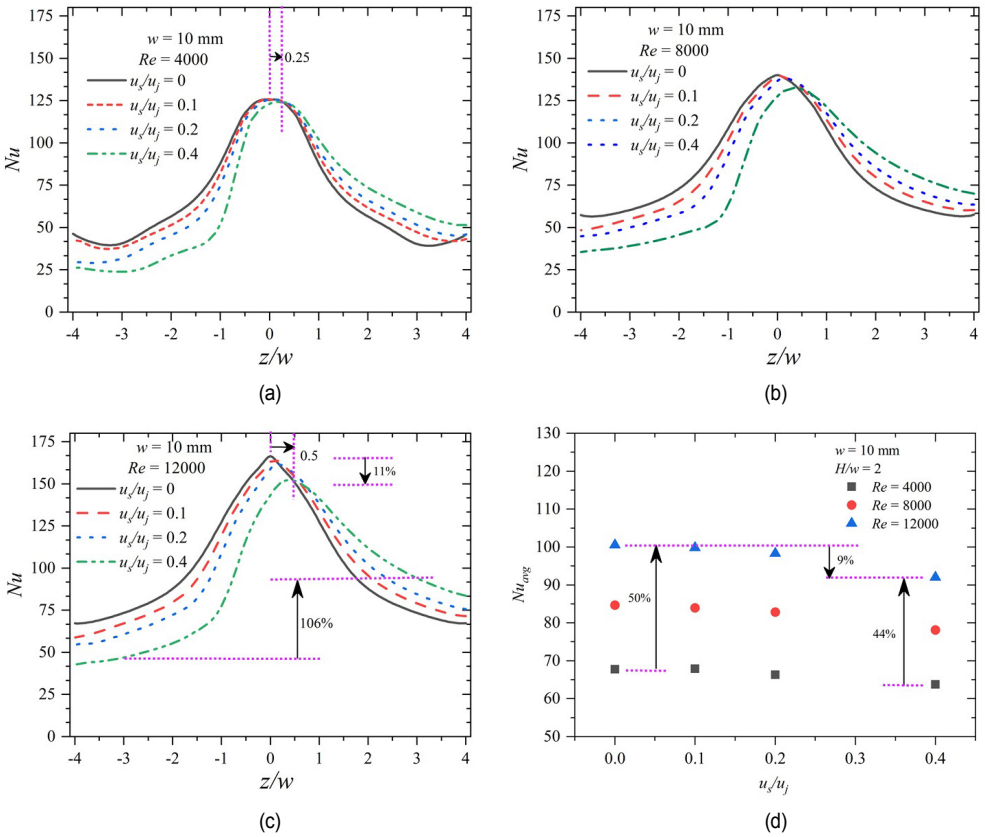

Fig. 6. Effect of surface velocity on local Nusselt number for (a) Re = 4000; (b) Re = 8000; (c) Re = 12000; (d) average Nusselt number for different Re and surface velocity.

film in the flow direction after $z/w \approx 1.5$, for the static surface case. Analogous to that, the Nusselt number profile changes slope, and it reduces with a relatively slower rate till $z/w \approx 3$ due to the increased effect of turbulence fluctuations. At $z/w \approx 3$, Nu curve attains a local minimum and then increases till $z/w \approx 4$. The changes in Nusselt number characteristics at downstream $3 \leq z/w \leq 4$ are associated with a hydraulic jump, as was shown in Fig. 4(b) (Sec. 3.1), and turbulence fluctuations, as was shown in Fig. 5 (Sec. 3.2). The hydraulic jump could cause higher turbulence fluctuations, inducing better mixing of hot and cold liquid. We also observed an increased level of turbulence fluctuations away from impact for static surface case as was depicted in Fig. 5 (Sec. 3.2). Coupled effect of these cause convective heat transfer to increase at $z/w \geq 3$ and $z/w \leq -3$.

For moving surface cases, unsymmetrical Nusselt number distribution is observed along both sides of the geometric center. For $u_s/u_j = 0.4$, the Nusselt number shows decreasing trends in the forward region. On the revere region, the Nusselt number decreases sharply till $z/w \approx -1$, after this, the slope of the Nusselt number changes, and it reduces with a slower rate till $z/w \approx -2.9$. Following this location, Nusselt number shows a nearly constant or slight increasing trend on the reverse side at $-4 \leq z/w \leq -2.9$. The changes in Nusselt number profile at location $z/w = -1$ are distinguishable for $u_s/u_j = 0.4$ compared to the static surface case and can be attributed to turbulence fluctuations. Qualitatively, it can be seen that the location after which the turbulence intensity starts to increase is associated with the change in the slope of the Nusselt number. As seen from the turbulence intensity distribution from Fig. 5 (Sec. 3.2), the location, after which turbulence intensity increases, was closer to the impact region for moving surface case than the static surface case on the reverse side. Due to increased turbulence intensity, the Nusselt number decreases with a relatively slower rate after location $z/w = -1$ in the reverse direction. Overall, the local Nusselt number is higher on the forward side than on the reverse side for moving surface cases. For instance, Nu value at $z/w = 3$ is 106 % higher than local Nusselt number at $z/w = -3$.

Moving surface affects the location corresponding to the peak value of the Nusselt number near the impact region. The location corresponds to peak Nusselt number shifts towards the forward side with increasing surface velocity. For the case of $u_s/u_j = 0.4$, the shifting distance is around 2.5 mm ($z/w = 0.25$). However, the peak values of the Nusselt number have marginal differences between static and moving surface cases for $Re = 4000$, as shown in Fig. 6(a). Away from the impact region, except for the region associated with the hydraulic jump, the Nusselt number increases with increasing surface velocity on the forward side. However, an opposite trend is observed in the reverse region. Here, it should be noted that the moving surface causes higher turbulence fluctuations on the reverse side, which should favor higher heat removal rate from the

impingement surface. Nevertheless, the moving surface, which has momentum in the positive *z* direction, provides resistance to liquid film flow. The overall effect of these phenomena is causing the Nusselt number to decrease with increasing surface velocity on the reverse side. On the forward region, the moving surface provides additional drag to the liquid layer and causes the liquid to move quickly. In other words, the liquid velocity on the forward region is higher than the reverse region. As a result, the heat removal rate increases with surface velocity on the forward region.

Fig. 6(c) shows the Nusselt number profiles for different surface velocity ratio cases of *Re* = 12000. The shift in the location corresponding to peak value of Nusselt number for u_s/u_j = 0.4 is higher as compared to *Re* = 4000 and u_s/u_j = 0.4. The difference in peak values of *Nu* of static and moving surface (u_s/u_j = 0.4) is around 11 %. The difference was significantly low for lower Reynolds number case as was shown in Fig. 6(a). Additionally, since the hydraulic jump is not observed for this case, the changes in heat transfer characteristics associated with it and its locations are not observed. For *Re* = 8000, Nusselt number profiles for different surface velocities are shown in Fig. 6(b). For *Re* = 8000 and *Re* = 12000, the local Nusselt number increase with surface velocity in forward region. However, opposite trends are observed on the reverse region. Effect of Reynolds number on heat transfer can be analyzed from Figs. 6(a)-(d) for different surface velocity cases. Nusselt number increases by increasing Reynolds number for all surface velocity ratio cases. For moving surface cases of u_s/u_j = 0.4, the differences in Nusselt number values are higher in forward region as compared to reverse region. For example, the difference in *Nu* values between *Re* = 12000 and *Re* = 4000 at *z*/*d* = 2 is around 39. However, at *z*/*d* = -2, this difference reduces to 21. Similar reductions in *Nu* values have been observed for other moving surface cases in comparison to static surface case.

Average Nusselt number is calculated by taking the mean value of local Nusselt number along z-axis (*x* = *y* = 0) as shown in Fig. 6(d). There is a slight reduction in average Nusselt number values for all Reynolds number cases with increasing surface velocity. For instance, the reduction is around 9 % as surface velocity increased to 0.4 from static surface case of *Re* = 12000. As can be seen from the local Nusselt number distribution in Figs. 6(a)-(c), reduction in heat transfer in reverse region contributes to overall Nusselt number reduction for moving surface cases. As in the forward region, the local Nusselt number increased with surface velocity. For a static surface case, incoming fluid directly interacts with the surface and removes heat load. However, with the surface in motion, incoming liquid has to interact with the moving liquid layer on the surface prior to interacting with the impingement surface. In other words, the liquid coming from the jet feels more resistance near the moving surface for the surface than the static surface case, especially on the reverse region. Overall, the average value of the Nusselt number increases with increasing Reynolds number. For *Re* = 12000, the average Nusselt number value for the static surface case is around 50 % higher than the *Re* = 4000 case. The difference reduces to 44 % for moving surface cases for u_s/u_j = 0.4, as highlighted in Fig. 6(d).

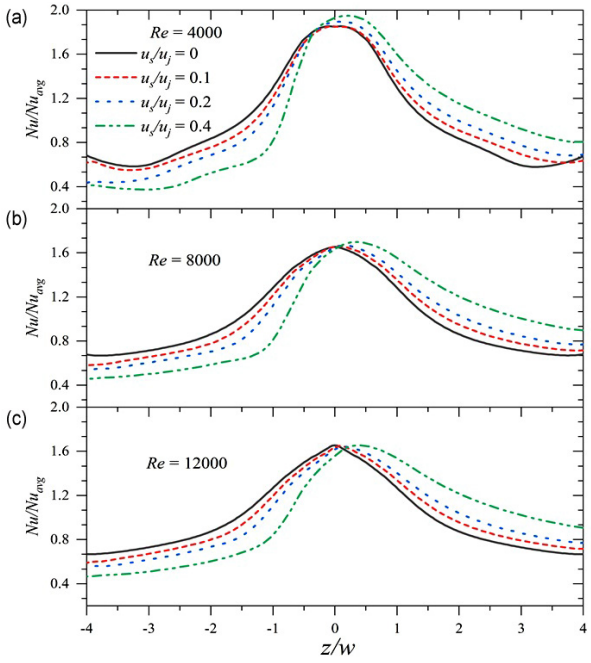

Fig. 7. Normalized Nusselt number for different surface velocity cases: (a) Re = 4000; (b) Re = 8000; (c) Re = 12000.

Figs. 7(a)-(c) show the ratio of local and average Nusselt number for different surface velocity ratio cases. Except near the impact region, Nusselt number ratio showed similar trends as were observed by the local Nusselt number distribution from Figs. 6(a)-(c). As clear from Fig. 7(a), peak value of Nu/Nu_{avg} increases with increasing surface velocity ratio for *Re* = 4000. However, for higher Reynolds number, the peak value of Nu/Nu_{avg} for moving surface cases remains nearly the same as static surface cases.

4. Conclusions

We presented a numerical study of free surface liquid jet impingement on a uniformly heated flat moving surface. Planer jet was considered due to its application in the sheet metal rolling industry. We used the domain splitting approach to perform 3D computations. In this method, we have divided the computation domain into two parts and then superimposed results as the boundary conditions. Results suggest that this approach has a potential to use for other applications where computation cost and time are major concerns. We used sale adaptive simulation (SAS) to model turbulent flow. To model the air-water interface, we used the volume of fluid (VOF) method. The present study considered three different Reynolds numbers (4000, 8000, 12000) based on nozzle exit conditions ($Re = \rho u_j w / \mu$) and four different surface velocity ratios (u_s/u_j). Focus has been given to understanding interfacial flow characteristics, turbulence intensity variations, and heat transfer relations. The following conclu-

sion can be drawn from the present numerical investigation.

1) Surface velocity has a negligible effect on jet thickness before impact. After impact, liquid film thickness reduces by increasing surface velocity in the forward region. Contrasting trends are observed on the reverse region, except for the region associated with the hydraulic jump for *Re* = 4000. In forward region, moving surface supported liquid film motion and hence increase mean velocity of liquid film, which resulted in lower film thickness. On the reverse side, moving surface oppose liquid film motion and hence film thickness increases with surface velocity. For all surface velocity cases, $0 \le u_s/u_j \le 0.4$, liquid film thickness increase with increase in Reynolds number owing to increased volume flow rate.

2) Local Nusselt number increases with surface velocity on the forward region due to increased mean velocity, which favors fast heat removal despite decreasing turbulence intensity. Conversely, *Nu* decreases with surface velocity on the reverse region. Reduced mean velocity has countered the effect of increasing turbulence fluctuation. The overall effect was a reduced heat transfer on the reverse region.

3) The shift in peak value of the Nusselt number from the geometric center was pronounced for *Re* = 12000 and u_s/u_j = 0.4. Moving surface affects the direction of liquid jet near the impact region and which results in shifted location of peak Nusselt number value. The difference in peak values of the Nusselt number increased with surface velocity, indicating significant effect of surface velocity on liquid film flow at higher u_s/u_j.

4) Local Nusselt number increase with increasing Reynolds number for all the surface velocity cases. The increase was more pronounced in the forward region due to added momentum of moving surface.

5) Average Nusselt number increases with increasing Reynolds number. However, it reduces with surface velocity. This means reduced heat transfer in reverse region has more dominant effect on overall Nusselt number then increased heat transfer in forward region. For *Re* = 12000. The reduction was around 9 % if the surface velocity ratio, u_s/u_j, increased to 0.4 from zero.

Acknowledgments

This research was supported by Basic Science Research Program through the National Research Foundation of Korea (NRF) grant, funded by the Korea government (MSIT) (No. 2020R1A2C3010568, 2021R1A6A1A03039696), and by the Bio & Medical Technology Development Program of the National Research Foundation funded by the Korean government (MSIT) (No. 2021M3A9I402294311). In addition, it was also supported by the Korea Environment Industry & Technology Institute (KEITI) through its Ecological Imitation-based Environmental Pollution Management Technology Development Project, and funded by the Korea Ministry of Environment (MOE) (20190027 90003).

References

[1] T. Altan, S. I. Oh and G. Gegel, Metal forming fundamentals and applications, *American Society for Metals*, 353 (1983).

[2] S. R. Choudhury and Y. Jaluria, Forced convective heat transfer from a continuously moving cylindrical rod undergoing thermal processing, *Proc. of Winter Annual Meeting of the American Society of Mechanical Engineers* (1992) 43-50.

[3] S. Polat, Heat and mass transfer in impingement drying, *Drying Technology*, 11 (6) (1993) 1147-1176.

[4] J. Shi, X. Qi, R. Liang and D. Zhang, Numerical study on the flow characteristics of slot cooling header after rolling, *Proc. of Journal of Physics: Conference Series*, 1885 (2021) 052016.

[5] M. L. Hosain, R. B. Fdhila and A. Daneryd, Multi-jet impingement cooling of a hot flat steel plate, *Energy Procedia*, 61 (2014) 1835-1839.

[6] Z. Xu, S. Wang, H. Wang, H. Song, S. Li and X. Chen, Effect of cooling rate on microstructure and properties of twin-roll casting 6061 aluminum alloy sheet, *Metals*, 10 (9) (2020) 1168.

[7] M. M. Amiri and F. Fereshteh-Saniee, An experimental investigation on the effect of cooling rate during combined continuous casting and rolling process on mechanical properties of 7075 aluminum alloy, *Transactions of the Indian Institute of Metals*, 73 (2) (2020) 441-448.

[8] M. L. Lobanov, M. L. Krasnov, V. N. Urtsev, S. V. Danilov and V. I. Pastukhov, Effect of cooling rate on the structure of low-carbon low-alloy steel after thermomechanical controlled processing, *Metal Science and Heat Treatment*, 61 (1) (2019) 32-38.

[9] H. Chattopadhyay and A. Cemal Benim, Turbulent heat transfer over a moving surface due to impinging slot jets, *Journal of Heat Transfer*, 133 (10) (2011) 1-5.

[10] B. Buonomo, O. Manca, N. S. Bondareva and M. A. Sheremet, Thermal and fluid dynamic behaviors of confined slot jets impinging on an isothermal moving surface with nanofluids, *Energies*, 12 (11) (2019) 1-20.

[11] S. Pawar and D. K. Patel, Study of conjugate heat transfer from the impingement of an inclined free slot jet onto the moving hot surface, *International Communications in Heat and Mass Transfer*, 111 (2020) 104429.

[12] M. Aghahani, G. Eslami and A. Hadidi, Heat transfer in a turbulent jet impinging on a moving plate considering high plate-to-jet velocity ratios, *Journal of Mechanical Science and Technology*, 28 (11) (2014) 4509-4516.

[13] S. Shah, Numerical analysis of heat transfer between multiple jets and flat moving surface, *International Journal of Heat and Mass Transfer*, 171 (2021) 121088.

[14] P. K. Kadiyala and H. Chattopadhyay, Numerical analysis of heat transfer from a moving surface due to impingement of slot jets, *Heat Transfer Engineering*, 39 (2) (2018) 98-106.

[15] M. R. Mohaghegh and A. B. Rahimi, Single- and two-phase water jet impingement heat transfer on a hot moving surface, *Journal of Thermal Analysis and Calorimetry*, 137 (4) (2019) 1401-1411.

[16] H. Chattopadhyay, G. Biswas and N. K. Mitra, Heat transfer from a moving surface due to impinging slot jets, *Journal of Heat Transfer*, 124 (3) (2002) 433-440.

[17] A. Chitsazan and B. Glasmacher, Numerical investigation of heat transfer and pressure force from multiple jets impinging

on a moving flat surface, *International Journal of Heat and Technology*, 38 (3) (2020) 601-610.

[18] A. Basaran and F. Selimefendigil, Numerical study of heat transfer due to twinjets impingement onto an isothermal moving plate, *Mathematical and Computational Applications*, 18 (3) (2013) 340-350.

[19] E. Ersayin and F. Selimefendigil, Numerical investigation of impinging jets with nanofluids on a moving plate, *Mathematical and Computational Applications*, 18 (3) (2013) 428-437.

[20] M. Rahimi and R. Azimi Soran, Numerical analysis of heat transfer and flow field due to slot air jet impingement for the cases of moving plate and moving nozzle, *Iranian Journal of Science and Technology, Transactions of Mechanical Engineering*, 41 (3) (2017) 217-224.

[21] H. Co¸sanay, H. F. Oztop and F. Selimefendigil, A computational analysis on convective heat transfer for impinging slot nanojets onto a moving hot body, *International Journal of Numerical Methods for Heat and Fluid Flow*, 31 (1) (2022) 364-386.

[22] R. Dutta, A. Dewan and B. Srinivasan, CFD study of slot jet impingement heat transfer with nanofluids, *Proceedings of the Institution of Mechanical Engineers, Part C: Journal of Mechanical Engineering Science*, 230 (2) (2016) 206-220.

[23] D. Singh, B. Premachandran and S. Kohli, Experimental and numerical investigation of jet impingement cooling of a circular cylinder, *International Journal of Heat and Mass Transfer*, 60 (2013) 672-688.

[24] M. A. Teamah, M. M. Khairat Dawood and A. Shehata, Numerical and experimental investigation of flow structure and behavior of nanofluids flow impingement on horizontal flat plate, *Experimental Thermal and Fluid Science*, 74 (2016) 235-246.

[25] A. Datta, S. Kumar and P. Halder, Heat transfer and thermal characteristics effects on moving plate impinging from cu-water nanofluid jet, *Journal of Thermal Science*, 29 (1) (2020) 182-193.

[26] M. Achari and M. K. Das, Conjugate heat transfer study of a turbulent slot jet impinging on a moving plate, *Heat and Mass Transfer*, 53 (3) (2017) 1017-1035.

[27] M. Rahimi and R. A. Soran, Slot jet impingement heat transfer for the cases of moving plate and moving nozzle, *Journal of the Brazilian Society of Mechanical Sciences and Engineering*, 38 (8) (2016) 2651-2659.

[28] M. A. Sharif and A. Banerjee, Numerical analysis of heat transfer due to confined slot-jet impingement on a moving plate, *Applied Thermal Engineering*, 29 (2009) 532-540.

[29] N. Rajaratnam, D. Z. Zhu and S. P. Rai, Turbulence measurements in the impinging region of a circular jet, *Canadian Journal of Civil Engineering*, 37 (5) (2010) 782-786.

[30] D. H. Wolf, R. Viskanta and F. P. Incropera, Turbulence dissipation in a free-surface jet of water and its effect on local impingement heat transfer from a heated surface: part 2-local heat transfer, *Journal of Heat Transfer*, 117 (1) (1995) 85-94.

[31] A. Datta, S. Kumar and P. Halder, Heat transfer and thermal characteristics effects on moving plate impinging from Cu-water nanofluid jet, *Journal of Thermal Science*, 29 (1) (2020) 182-193.

[32] K. Baghel, A. Sridharan and J. S. Murallidharan, Experimental and numerical study of inclined free surface liquid jet impingement, *International Journal of Thermal Sciences*, 154 (2020) 106389.

[33] K. Baghel, A. Sridharan and J. S. Murallidharan, Numerical study of free surface jet impingement on orthogonal surface, *International Journal of Multiphase Flow*, 113 (2019) 89-106.

[34] R. Maliska, E. E. Paladino, F. Saltara, B. A. Contessi and R. Ataides, A comparison of turbulence models for the computation of a detached flow around a square cylinder, *Proc. of 20th Annual Conference of Computational Fluid Dynamic Society of Canada*, Canada (2012) 9-11.

[35] Y. Egorov and F. Menter, Development and application of SST-SAS turbulence model in the DESIDER project, *Proc. of Advances in Hybrid RANS-LES Modelling*, Berlin (2008) 261-270.

[36] F. R. Menter, M. Kuntz and R. Bender, A scale-adaptive simulation model for turbulent flow predictions, *Proc. of 41st Aerospace Sciences Meeting and Exhibit* (2003) 767.

[37] F. R. Menter and Y. Egorov, The scale-adaptive simulation method for unsteady turbulent flow predictions. part 1: theory and model description, *Flow, Turbulence and Combustion*, 85 (1) (2010) 113-138.

[38] W. Zheng, C. Yan, H. Liu and D. Luo, Comparative assessment of SAS and DES turbulence modeling for massively separated flows, *Acta Mechanica Sinica*, 32 (1) (2016) 12-21.

[39] W. Hirt and B. D. Nichols, Volume of fluid (VOF) method for the dynamics of free boundaries, *Journal of Computational Physics*, 39 (1) (1981) 201-225.

[40] J. U. Brackbill, D. B. Kothe and C. Zemach, A continuum method for modeling surface tension, *Journal of Computational Physics*, 100 (2) (1992) 335-354.

[41] J. Laufer, *The Structure of Turbulence in Fully Developed Pipe Flow*, NACA Report 1174 (1952).

[42] J. Nikuradse, Gesetzmassigkeiten der turbulenten Stromung in glatten Rohren, *Ver Deutsch. Ing. Forschungsheft*, 356 (1932).

[43] K. Ibuki, T. Umeda, H. Fujimoto and H. Takuda, Heat transfer characteristics of a planar water jet impinging normally or obliquely on a flat surface at relatively low Reynolds numbers, *Experimental Thermal and Fluid Science*, 33 (8) (2009) 1226-1234.

[44] T. Vader, F. P. Incropera and R. Viskanta, Local convective heat transfer from a heated surface to an impinging, planar jet of water, *International Journal of Heat and Mass Transfer*, 34 (3) (1991) 611-623.

[45] Y. Chen, C. Ma, M. Qin and Y. Li, Theoretical study on impingement heat transfer with single-phase free-surface slot jets, *International Journal of Heat and Mass Transfer*, 48 (16) (2005) 3381-3386.

[46] H. Wolf, R. Viskanta and F. P. Incropera, Local connective heat transfer from a heated surface to a planar jet of water with a nonuniform velocity profile, *Journal of Heat Transfer*, 112 (1990) 899-905.

[47] M. Kuraan and K. Choo, The influence of nozzie-to-plate spacing on the circular hydraulic jump of water jet impingement, Proc. of *16th IEEE Intersociety Conference on Thermal and Thermomechanical Phenomena in Electronic Systems* (2017)

86-89.
[48] K. Choo and S. J. Kim, The influence of nozzle diameter on the circular hydraulic jump of liquid jet impingement, *Experimental Thermal and Fluid Science*, 72 (2016) 12-17.
[49] J. Stevens and B. W. Webb, Measurements of flow structure in the radial layer of impinging free-surface liquid jets, *International Journal of Heat and Mass Transfer*, 36 (15) (1993) 3751-3758.

Kuldeep Baghel is a post-doctor at the school of Mechanical Engineering, Sungkyunkwan University, Suwon, Korea. He received his Ph.D. in Mechanical Engineering from the Indian Institute of Technology Bombay, Mumbai, India. His research interests include microfluidics, heat and mass transfer and interfacial flow phenomena.

Zahra is a graduate (M.S.-Ph.D. combined) student of the School of Mechanical Engineering, Sungkyunkwan University, Suwon, Korea. She received her B.S. in Mechanical Engineering from the Pakistan Institute of Engineering and Applied Sciences. Her research interests include microfluidics, heat transfer, electrohydrodynamics, and droplet generation.

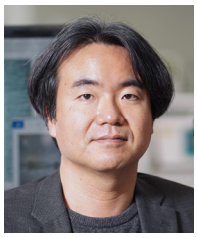

Jinkee Lee received his B.S. and M.S. degrees from Korea Advanced Institute of Science and Technology, and his Ph.D. from Brown University, USA. Since 2012, he has been a Professor at the School of Mechanical Engineering and Institute of Quantum Biophysics of Sungkyunkwan University, Korea. His research interests include interfacial flow, microfluidics, biomimetics, and biofluids.